Available online at www.sciencedirect.com
SCIENCE DIRECT®
Sensors and Actuators A 121 (2005) 566–575
SENSORS AND ACTUATORS A PHYSICAL
www.elsevier.com/locate/sna

A microfabricated electromagnetic linear synchronous motor

M.V. Shutov [a], E.E. Sandoz [a], D.L. Howard [a], T.C. Hsia [a], R.L. Smith [b], S.D. Collins [b,*]

[a] *Department of Electrical Engineering, University of California, Davis, CA, USA*
[b] *MicroInstruments and Systems Laboratory, University of Maine, Orono, ME, USA*

Received 28 May 2004; accepted 8 March 2005
Available online 17 May 2005

Abstract

A miniature linear synchronous motor was designed, fabricated and tested. Actuation was achieved through interaction of traveling magnetic wave, generated by linear array of microcoils on the stator, and permanent magnets on the rotor. Two configurations of the motor were investigated. One with a single hand-assembled permanent magnet on rotor and corresponding array of multiturn microcoils; the other, a fully microfabricated rotor with embedded array of screenprinted permanent magnets and a linear array of serpentine microcoils on the stator. Motion of the rotor was constrained by dovetail microjoints. A numerical model was developed for modeling and dynamic control. The motor was tested under various operating conditions with both open- and closed-loop control. The motors showed reliable translation over 6 cm travel with accuracy limited by the feedback system.

Keywords: Electromagnetic; Actuator; LSM; Microsystem; Micromotor; Control

1. Introduction

An unquenchable interest in long-range microactuators is fueled by critical microinstrument applications, such as optical positioning [1], robotics [2], surgery [3], etc. These applications not only demand the precision translation inherently found in microfabricated systems, but also require extended actuation distances of millimeters to centimetres—a requirement not normally associated with microsytems. Several types of long-range microactuation mechanisms have been reported, each showing varying degrees of success: piezoelectric [4,5], electrostatic [6], and electromagnetic [7–9]. However, both electrostatic and piezoelectric actuators require complex mechanisms to parley their inherently short-range actuation mechanisms into long-range translation.

Linear electromagnetic actuators, on the other hand, are inherently long-range devices due to extended electromagnetic fields and should serve well as a transduction mechanism for long-range actuators. Additionally, electromagnetic actuators utilizing permanent magnets on the motive components eliminate the need for electrical connections to moving components, and thereby reduce complexity. A diverse number of magnetic actuators for various special applications have been demonstrated using electroplated soft magnetic materials such as FeNi [10], commercial permanent magnets [7–9,11], electroplated CoNiMnP permanent magnets [12], or screen-printed polymer magnets [13]. Additionally, long-range linear magnetic actuators utilizing relatively large commercial permanent magnets [7–9,14] have also been demonstrated, as well as proposed methods to integrate magnetic components into the microfabrication arena using electroplated or screen plated permanent magnets [12,13,15]. However, to date, none of these techniques have been applied to a fully microfabricated long-range linear translation actuator.

This paper presents a miniature three-phase linear synchronous motor, LSM, predicated upon a derivation of the more familiar macro magnetic levitation, i.e. (MagLev) trains [16]. Two miniature linear synchronous motor designs are presented and characterized. Moving components of both motors are made passive using permanent magnets, to meet the performance and fabrication specifications for the applications stated above. To analyze the performance of both LSM designs, a dynamic model was developed and pre-

* Corresponding author. Tel.: +1 207 5812269.
E-mail address: scott.collins@maine.edu (S.D. Collins).

0924-4247/$ – see front matter © 2005 Elsevier B.V. All rights reserved.
doi:10.1016/j.sna.2005.03.022

sented. To further improve the positioning performance of both LSMs, a feedback controller was implemented to compensate for frictional forces and non-linear LSM dynamics.

2. LSM concept of operation and motors layout

Linear synchronous motors, LSMs, are simply electromagnetic motors used for linear rather than rotary motion. Several different LSM variants exist with most of them relying on the interaction between a magnet, permanent or electromagnetic on a rotor, and a traveling electromagnetic wave produced by stator. In a typical three-phase LSM operation, three arrays of coils on the stator excite a phased spatial distribution of electromagnetic fields that propagates along the length of the stator. The permanent magnet on the rotor, the translational stage in this case, essentially follows the traveling wave by mutual interaction between the two magnetic fields.

In this paper, two miniature LSM designs were fabricated as shown in Fig. 1. Both LSM designs employ dovetail microjoints for low runout translation [17], permanent magnets on the rotor, and a three-phase microcoil array on the stator. However, in the LSM1 design, the stator is composed of a linear array of multiturn microcoils and the rotor uses a single, high-field NdFeB permanent magnet; while in the LSM2 design, the stator is composed of a serpentine microcoil array while the rotor provides a matching integrated permanent magnet array. Preliminary work on LSM1 design has been reported previously [18]. It consists of a linear array of six-turn microcoils for the stator and a large button permanent magnet manually attached to the rotor. Although initial testing of LSM1 generated large translational forces, the large permanent magnet did not provide a convenient mechanism to scale the LSM. Therefore, another more integrated LSM design, LSM2 was introduced. The stator for the LSM2 has a three-phase array of serpentine planar coils that matches the period of permanent magnets fabricated into the rotor of LSM2. Table 1 provides a list of the key parameters for both LSM1 and LSM2 designs.

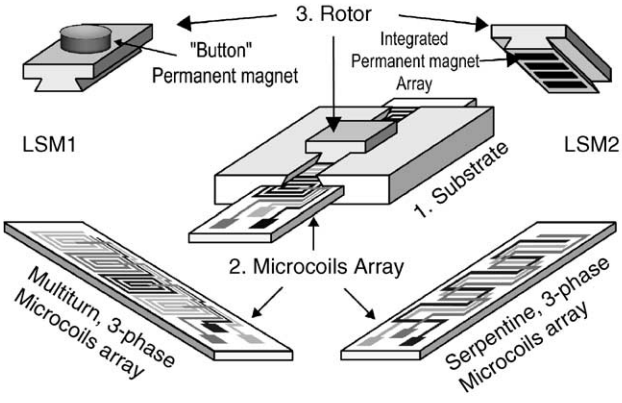

Fig. 1. Micro LSM assembly. LSM1 (left) shows a simple design using a single permanent "button" magnet and an array of multiturn microcoils. LSM2 (right) shows a more integrated version with integrated permanent magnets and a serpentine microcoil array.

Table 1
Design data of LSM

Specification data	LSM1	LSM2
Coil type	Multiturn	Serpentine
Microcoil pole pitch τ (mm)	11.7	1.95
Number of turns per coil	6	1
Track length (mm)	60	60
Single-current conductor width (μm)	300	300
Distance between each conductor (μm)	325	325
Permanent magnet type	"Button" NdFeB	Screen printed NdFeB paste
PM magnetization (A/m)	6.4×10^5	1.4×10^5
Magnet length/width/height (mm)	6/6/4	0.8/2.5/0.35
Number of magnets in array	1	6
Distance between coils and magnets d (μm)	900	50–100

3. Fabrication

Both LSM designs were fabricated as three separate components and later assembled into the finished actuator. The three components are labeled in Fig. 1 as: (1) substrate which houses the dovetail tracks and provides a platform for the facile assembly of the LSM; (2) stator or electromagnetic microcoil array; and (3) rotor translational microstage, with button magnet or integrated permanent magnets for the two LSM designs.

3.1. Substrate fabrication

The LSM substrate was fabricated as a three-wafer silicon stack (Fig. 2). The substrate provides support and alignment for the microcoil array, as well as provides dovetail bearing

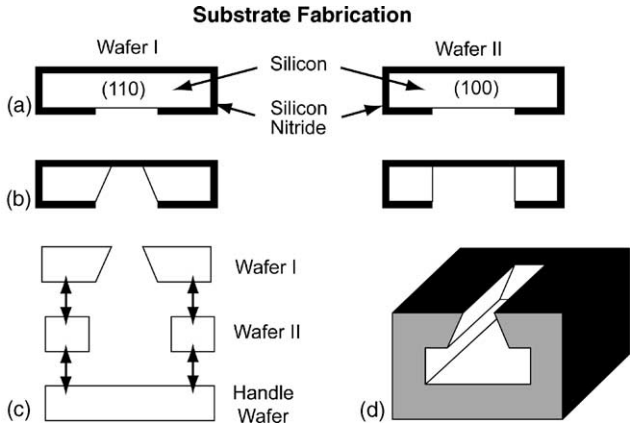

Fig. 2. Process flow for substrate fabrication: (a) LPCVD silicon nitride is deposited and patterned on two separate silicon wafers; (b) wafers are anisotropically etched in KOH to form dovetail joint (left) and microcoil array slot (right); (c) wafer I, wafer II, and a handle wafer are fusion bonded together; (d) completed substrate is covered with LPCVD silicon nitride.

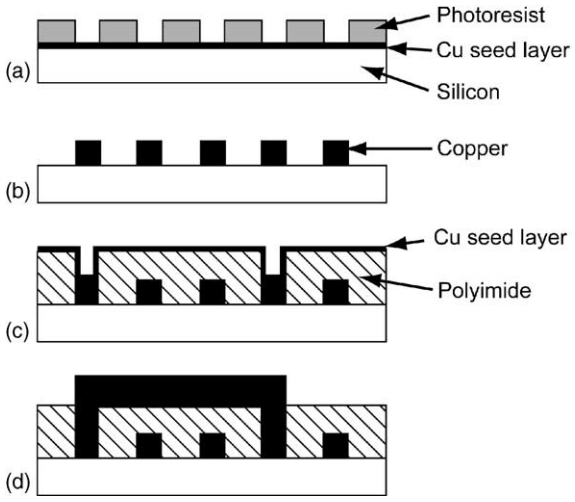

Fig. 3. Process flow of microcoil fabrication: (a) copper seed layer is deposited, photoresist is applied and photopatterned; (b) copper is electroplated, photoresisted and seed layer are removed; (c) polyimide is applied and patterned, seed layer for second metalization layer is deposited; (d) cross-section of fabricated microcoil with two metalization layers and crossovers.

surfaces for the rotor translation. As shown in Fig. 2(a), silicon wafers I and II were covered with a 120 nm LPCVD silicon nitride etch mask that is patterned using conventional photolithography and RIE etching. The wafers were then anisotropically etched in 45% KOH at 60 °C (Fig. 2(b)). Mask alignment to either the (1 1 0) or (1 0 0) planes, respectively, creates the familiar 54.4° side walls of wafer I or the vertical side walls of wafer II. wafers I and II were aligned and fusion bonded with a silicon handle wafer at 1100 °C in O_2 for 2 h (Fig. 2(c)). The entire wafer stack is then coated with a 120 nm LPCVD silicon nitride film. Fig. 2(d) shows the final assembly.

3.2. Stator and microcoil fabrication

The stator and microcoil arrays were fabricated on a separate silicon wafer using a multi-level metallization process. Microcoil fabrication started with an e-beam evaporation of 10 nm titanium/100 nm copper seed layer on top of a 200 nm silicon oxide coated silicon wafer (Fig. 3(a)). A 10 μm thick layer of photoresist AZ4620 (Hoechst-Celanese) was photolithographically patterned creating the mold for electrodeposition of the first metal layer. The wafer was then immersed in a Cu plating bath, Technic Inc. "Cupper-U", and copper electroplated at a constant current of 25 mA/cm^2 to a thickness of 10 microns using a Cu anode. The photoresist was then stripped and the seed layer removed by a quick dip in 1:1:20 solution of acetic acid/H_2O_2/water to remove the copper followed by a dip in 1:10 HF/water to remove the titanium adhesion layer (Fig. 3(b)).

Metal crossovers were then fabricated to electrically interconnect the microcoils. A 5 μm polyimide layer, HD Microsystems PI5878, was spun and patterned on the wafer to form a dielectric spacer between the metal layers (Fig. 3(c)), and a second Cu metallization was fabricated by repetition of steps 3(a) and 3(b). The cross sectional diagram of the final microcoil array structure complete with two-layer Cu metallization is shown in Fig. 3(d). This basic fabrication process was used for both the multiturn microcoils and the serpentine microcoil geometries. Shown in Fig. 4 are plan view photographs of completed three-phase microcoil arrays: (1) multiturn microcoils; (2) Serpentine microcoils; and (3) complete microcoil array diced into a strip for insertion into the substrate slot. Bonding pads are shown at the ends of the strip for electrical connection to the microcoils. Fabricated microcoils had a typical resistance of 2.8–3 Ω for the serpentine configuration and 6–8 Ω for the multiturn configuration.

3.3. Rotor fabrication

For both LSM configurations, the rotor utilizes a dovetail microjoint to precisely constrain motion and provide low runout. For LSM1, the rotor followed the same fabrication procedures given in reference [17]. After rotor fabrication, a 6 mm diameter NdFeB "button" magnet was adhesively attached to the top of the rotor.

The dovetail fabrication process for LSM2 rotor followed a similar process to the LSM1 rotor, but was modified slightly to provide integration of a permanent magnet array in the bottom of the rotor. The LSM2 rotor fabrication process is shown in Fig. 5. Two (1 0 0) silicon wafers, I and II, were anisotropically etched in 45% KOH at 60 °C using a silicon nitride mask (Fig. 5(a)). Wafer II was etched to termination, while a 150 μm membrane was left on wafer I for future wafer bonding. The dimensions and spacing for openings in wafer II were determined by the motor parameters given in Table 1. The wafers were then aligned, fusion bonded together, and coated with a 150 nm LPCVD silicon nitride film (Fig. 5(b)). A 10 nm titanium/100 nm gold seed layer was e-beam evaporated and photoresist patterned to expose the KOH etched recess (Fig. 5(c)). A 300 μm Permalloy (80% Ni/20% Fe) core was electroplated into the recess as shown in Fig. 5(d). The plating solution and detailed NiFe electroplating procedure is given elsewhere [19,20]. Electroplating was performed at current density of 15 mA/cm^2 using an Ni mesh as the anode. Permalloy deposited at rate of 10 μm/h. Magnetic properties of the Permalloy core were measured by a vibrating sample magnetometer recording magnetic moment M as a function of the applied field. From these measurements, the relative permeability μ_r was calculated to be 500. The permalloy was then polished and individual rotors were diced (Fig. 5(d)).

An epoxy suspension of a premagnetized powder, NdFeB with particle size 1–10 μm was then screenprinted into the bottom center recesses of the rotor (Fig. 5(e)). Based on weight measurements, the concentration of magnetic powder in epoxy suspension was found to be approximately 70%. Alternating polarity of the magnetic array was achieved by screenprinting alternate recesses and allowing the epoxy to cure in the presence of an external magnetic field, $H = 2 \times 10^4$ A/m. The external magnetic field was insuffi-

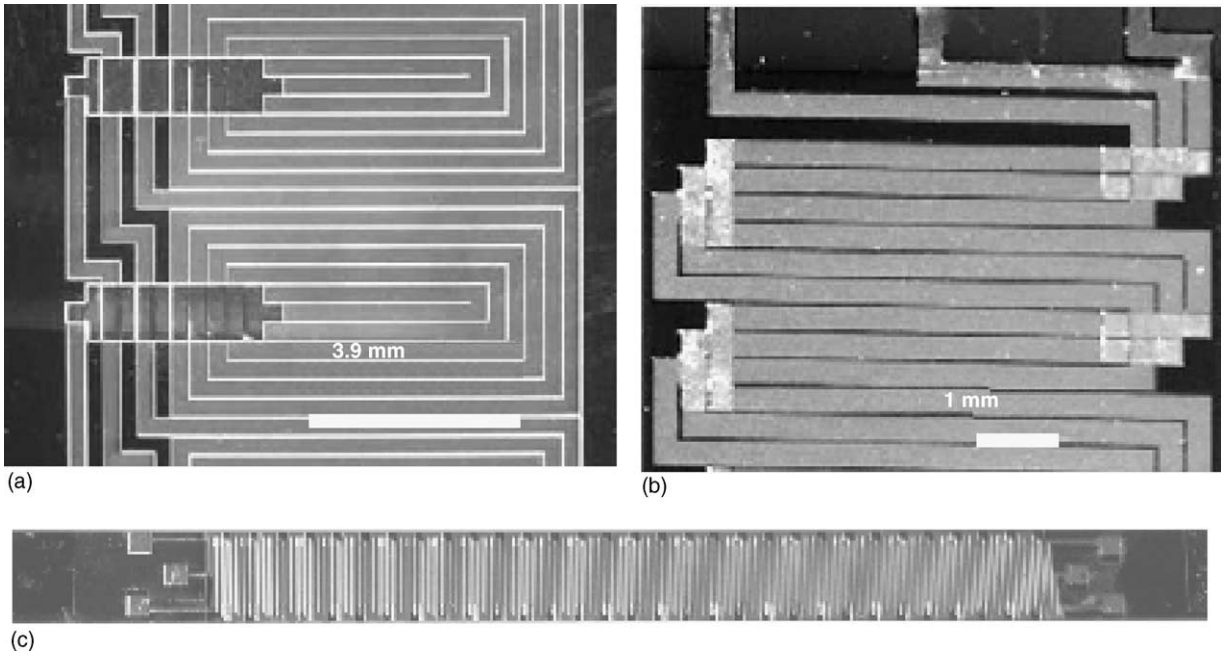

Fig. 4. Photograph of two microcoils array. (a) (Left) enlargement of multiturn coil design showing two six-turn spiral microcoils. Metal crossovers from the center of the coil to the exterior are shown on the left of the photo. (b) (Right) enlargement of serpentine microcoil design. The Cu lines serpentine down the length of the strip crossing over the other two phases at each end. (c) An entire microcoil array showing bonding pads at each end of the strip for electrical connections. Total length of the array is roughly 70 mm.

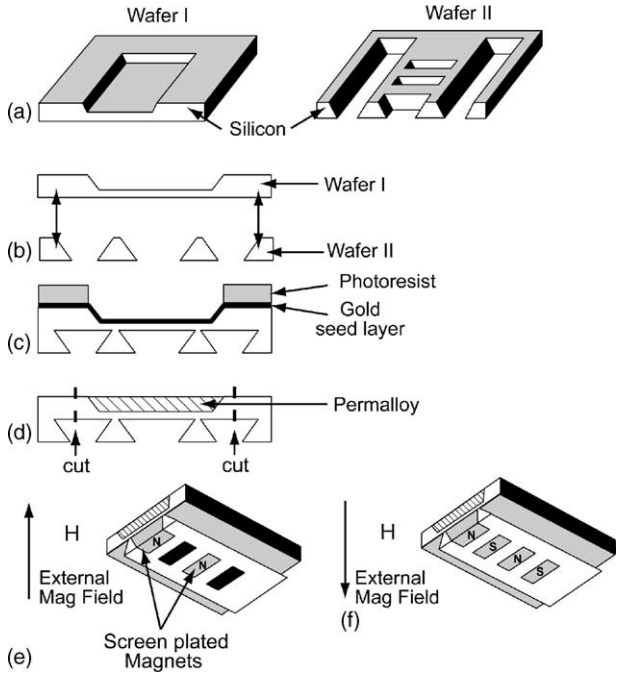

Fig. 5. Rotor fabrication flow: (a) two silicon wafers coated with LPCVD silicon nitride are patterned and anisotropically etched in KOH; (b) wafer I and wafer II are aligned and fusion bonded; (c) gold seed layer is deposited and patterned; (d) permalloy is electroplated, polished, and translational microstages are individually diced; (e) every other bottom recess is screen-plated with NdFeB/epoxy suspension in presence of an external magnetic field; (f) the rest of permanent magnets is screen-plated in presence of external magnetic field of opposite polarity.

cient to demagnetize the particles, but sufficient to orient the magnetic particles during curing. The remaining recesses were screenprinted and allowed to cure with a magnetic field of opposite polarity. The final rotor configuration with alternating permanent magnets is shown in Fig. 5(f). After the permanent magnets were fabricated, the individual rotors were assembled into the LSM. To measure magnetization of the screen-plated permanent magnets, test samples were fabricated under the same conditions as the rotors.

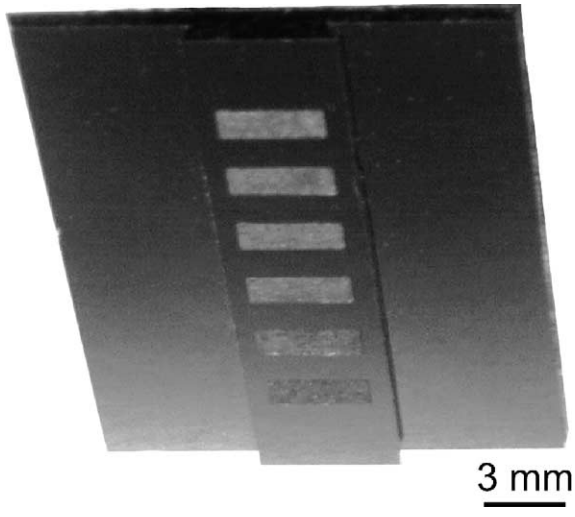

Fig. 6. Photograph of rotor with embedded permanent magnets. Photograph shows the bottom of the microstage with dovetail bearing microjoints and screen printed magnets.

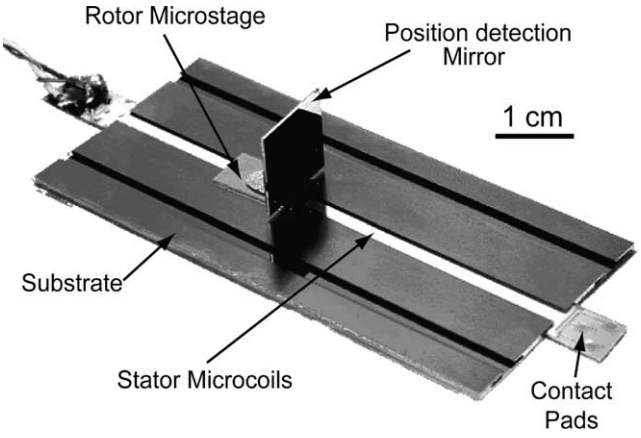

Fig. 7. Photograph of an assembled LSM microsystem complete with substrate, rotor (microstage), and stator (microcoils).

Magnetization was measured with a vibrating magnetometer giving $M = 1.4 \times 10^5$ A/m. Shown in Fig. 6 is a photograph of the translational rotor with dovetail joint bearings and array of embedded permanent magnets. The completely assembled LSM with substrate, rotor, and microcoil array is shown in Fig. 7.

4. Modeling and simulations

To assess the performance of both micromotor designs, numerical analysis of the field and force distributions were carried out using well-established theoretical models. Symmetry reduced all simulations and calculations to their respective 2D field distributions along the longitudinal cross section through the center of the coils as shown in Fig. 8. Fringe effects on either side of the microcoil array were assumed negligible and ignored. The fundamental unit for the model was the magnetic field generated by a fixed current i_k flowing in the z-direction through a single, infinitely long strip of conductive copper of fixed width, a, and negligible thickness centered around x_k. The magnetic field for different microcoil arrays was constructed by superposition of the fields generated from the appropriate number and arrangement of conductive strips each supporting the appropriate current.

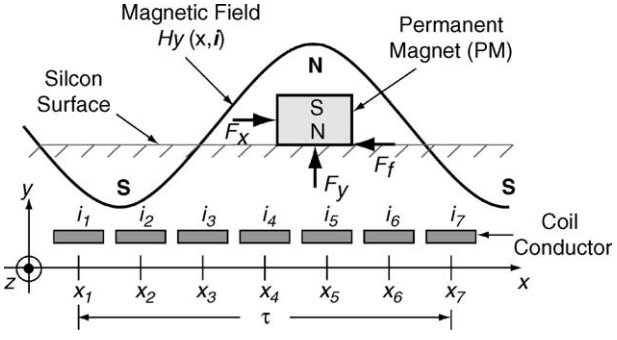

Fig. 8. Diagram of key LSM actuator components for concept of operation. $x_1, \ldots x_n$ are the x placements of the individual microcoil conductors; $i_1, \ldots i_n$ are the current associated with the x_nth specific conductor. F_x and F_y are the respective x and y field induced forces. F_f is the frictional force retarding motion, and τ is the pitch of the microcoils.

A phased, time variant, sinusoidal current input to each stator coil generates the equivalent spatial sinusoidal magnetic field along the length of the array as shown in Fig. 8. This field propagates in the x-direction with synchronous velocity:

$$V_s = \tau f, \tag{1}$$

where f is excitation current frequency and τ is the armature coil pole pitch. The permanent magnet, PM, located on the rotor follows the traveling armature field distribution. The force that serves to translate the rotor is governed by the strength of the permanent magnet and the armature field.

In the case of a single permanent magnet with magnetization $\vec{M}$, the force acting on it in the stator field $\vec{H}$, generated by the stator coils can be calculated by integration of the force density:

$$\vec{f} = \vec{\nabla}(\vec{M} \cdot \vec{H}) \tag{2}$$

over the volume of the permanent magnet V. For both designs, the magnetization of the permanent magnets is constant and has only one-directional component M_y. It follows then from (2) that the longitudinal and normal components of the force acting on the magnet are

$$F_x = M_y \int_V \frac{\partial}{\partial x} H_y(x, y)\, \mathrm{d}V, \quad F_y = M_y \int_V \frac{\partial}{\partial y} H_y(x, y)\, \mathrm{d}V \tag{3}$$

Magnetization in the y-direction gives a translational force dependence only on the y-component of the stator field $H_y(x, y)$. The y-component of the field generated by a single conductor is given as follows [21]:

$$H_y^k(x, y) = \frac{i_k}{8a\pi} \ln \left(\frac{(x - x_k + a)^2 + (y - y_k)^2}{(x - x_k - a)^2 + (y - y_k)^2} \right)^{1/2} \tag{4}$$

where a is the width of a single conductor, and $H_y^k(x, y)$ is the y-component of the stator field at a point (x, y) in the xy-plane due to the k^{th} current i_k flowing in a conductor centered at (x_k, y_k) (see Fig. 8). The resultant y-component of the stator field from all conductors at a point (x, y) given as:

$$H_y(x, y) = \sum_{k=1}^{N} H_y^k(x, y)$$

Fig. 9 shows the y-component of the stator field $H_y(x, y)$ at a fixed time for both LSM designs as a function of x and y. The x-axis, Track, covers two pole pitches along the microcoil array and the y-axis, Height, extends to the maximum height of the permanent magnets for both LSM designs. The x-axis is normalized to the number, N, of pole pitches, τ, to compensate for the differing microcoil designs (see Table 1). Also note

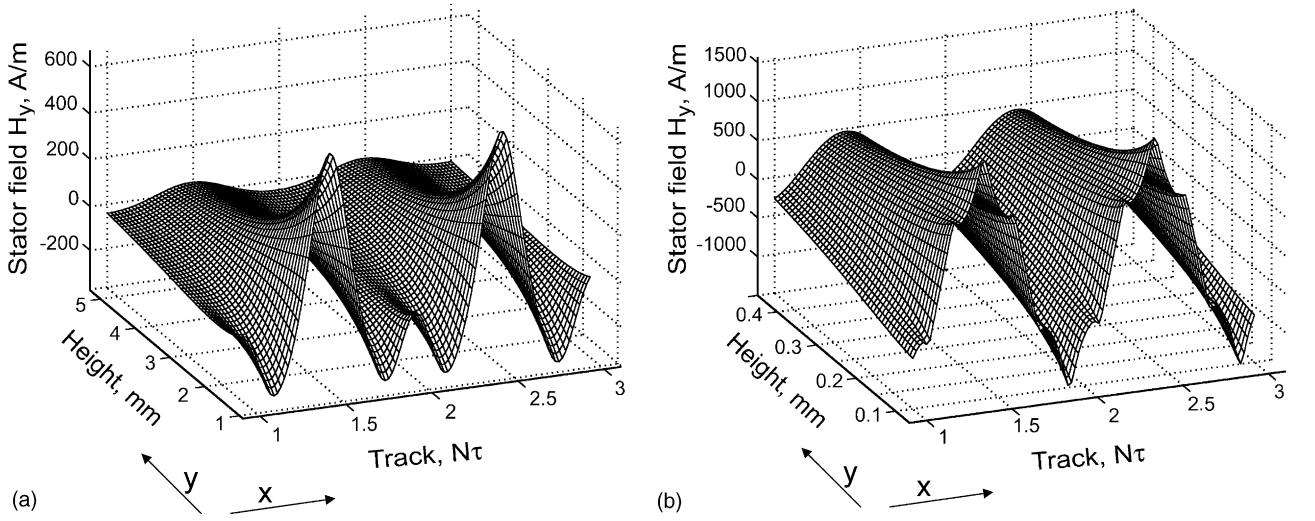

Fig. 9. Stator magnetic field distribution over two pole pitches for both LSM designs. The track axis records the distance along the microcoil array, and the height axis reflects the field strength at a distance above the microcoils: (a) field distribution for LSM1 and (b) field distribution for LSM2.

that the bottom of the button magnet of LSM1 is at 1 mm, which is much larger than that for LSM2.

As it can be seen in Fig. 9(a), for LSM1, the field shape is far from an ideal sinusoidal in the near-field region, i.e. for short microcoil/permanent magnet separations, although the field distribution is sinusoidal at the top of the magnet in the far-field regime. Since the near-field components will contribute more significantly to the motive force than the far-field, similar non-linearities can be anticipated in the operation of LSM1 design. By comparison, the stator field distribution of LSM2 is shown in Fig. 9(b). Though the LSM2 magnet is much closer to the coils with a distance starting at less than 0.1 mm above the conductors, the field shows that the near-field effects over the magnet are much less significant than for the LSM1 coil design.

Unfortunately, the shape of the stator field for both designs still deviates significantly from a sinusoidal as $H_y(x, y)$ translates, particularly in the near-field regime. The effect of stator field deviations on the motive force during translation is shown in Fig. 10, where the total motive force is graphed as a function of the "real" x_r, and desired position, x_d, of the rotor for the appropriate three-phased sinusoidal coil excitation. The desired position, x_d, is defined as the point where the rotor should be at the moment of time t, moving with synchronous velocity V_s, i.e. $x_d = V_s t$, or as it follows from Eq. (1) $x_d = \tau f_s t$, i.e. the x_d-axis is proportional to time. The real position, x_r, is the actual position at time, t. A semi-transparent plane is shown in both graphs representing the plane of perfect tracking, $x_r = x_d$. To maintain perfect tracking, i.e. a constant velocity in this case, the motive force acting on the rotor must be constant. However, it is seen in Fig. 10 that the force changes in a roughly sinusoidal fashion for both LSM designs along the plane of perfect tracking. It is therefore impossible for the rotor to perfectly track the desired position trajectory when excited with simple sinusoidal open-loop current inputs. However, the form of the deviations suggest

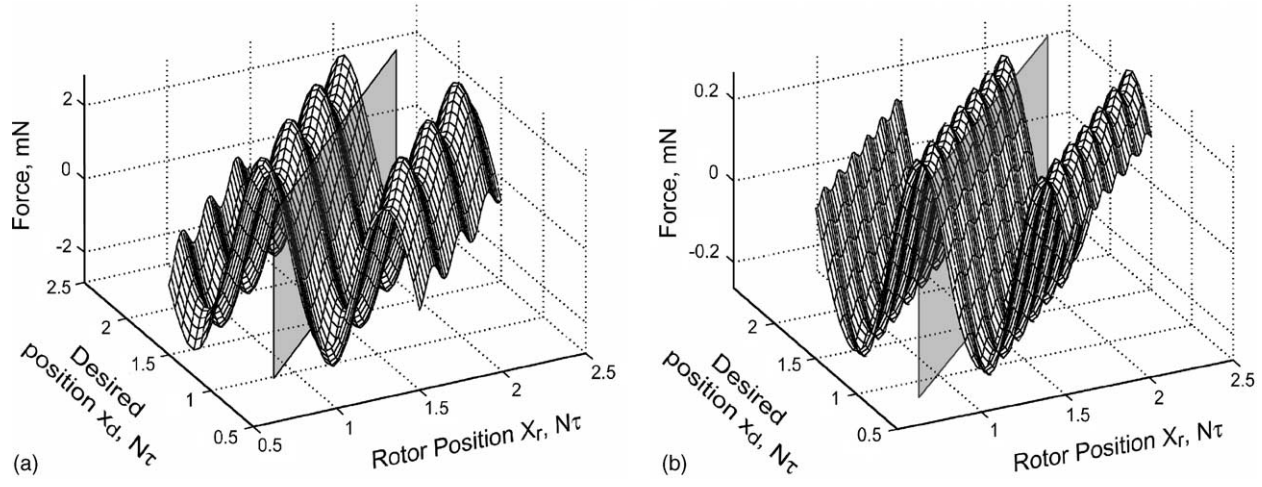

Fig. 10. Force distribution as a function of real and desired position for (a) LSM1 and (b) LSM2.

a control waveform, as will be discussed in subsequent sections.

Fig. 10(b) shows the force distribution for LSM2 with an array of six integrated magnets. The total force produced by the commercial button magnet of LSM1 (Fig. 10(a)) is greater than that of the integrated magnet array of LSM2; however, the relative force variations of LSM2 along $x_r = x_d$ are smaller in amplitude than LSM1. Within one-pole pitch, there are three force ripples for LSM1 design and six ripples for LSM2 design, which is due to different coil designs, multiturn versus serpentine. The pole pitch of LSM2 is also five-times smaller than that of LSM1. The result is a more frequent but smaller force ripple, when the rotor of the LSM2 is moving, while LSM1 exhibits a larger and less frequent force ripple. The force ripple's effect on LSM position trajectory is shown in Section 5.

Two frictional forces are considered in the model, viscous friction that is a linear frictional force, and a non-linear Coulombic frictional force. The total force of friction is given as

$$F_f = -\mu_{vf}|v_r| - \text{sign}(v_r)\mu_k|F_y - mg|$$

The coefficient of viscous friction is given by μ_{vf}, and the coefficient of kinetic friction is given by μ_k. When the velocity is zero, static friction dominates and μ_k is replaced by μ_s. The net force acting on the rotor magnet is then

$$F_{net} = \dot{V}_r m = F_x + F_f$$

Thus far, an intuitive description of the behavior of the LSM has been presented along with the foundation of the dynamic equations. It has also been shown that open-loop operation of the LSM cannot provide performance that is expected from the ideal LSM motor. Thus, closed-loop control of the device is required for accurate positioning.

5. Results and discussion

Physical performance such as linear translation and conveyable mass were investigated to evaluate the LSM characteristics. Position of the moving stage was determined by reflecting a HeNe laser beam off a corner cube (retro reflector) mounted on the rotor to a position sensitive diode (PSD). As the rotor moves, the reflected beam is scanned across the PSD and the diode voltage is then mapped to the rotor's position. Data acquisition and control of the three-phase driving current was accomplished using a computer.

5.1. Open-loop operation

To determine open-loop operation performance, the motors were driven by a constant frequency three-phase sinusoidal current. The motors are capable of smooth controlled operation between speeds of 0.1 and 8 cm/s. For both LSM designs, the total translation distance of the moving stage was 6 cm and was limited only by the wafer size that was used for substrate fabrication.

For LSM1, translation was observed at peak currents less than 600 mA. However, this generally resulted in a pulsating motion (i.e. jumping from coil to coil rather than smooth translation). Smoother motion was observed at currents higher than 900 mA. With a 0.5 g retro reflector attached to the rotor, LSM1 showed smooth translation at approximately 1.2 A. The operation of LSM2 started at 400 mA, but due to lower magnetization of microfabricated magnets, it required peak currents at around 1.2 A to operate with a retro reflector.

Fig. 11 compares the simulation of the dynamic model with the experimental results. Position versus time characteristics were obtained at driving current amplitude $I_0 = 1.2$ A for both LSM designs. Two different velocities shown to emphasize various aspects of motion for each design. Velocity was changed by changing the driving sinusoidal currents

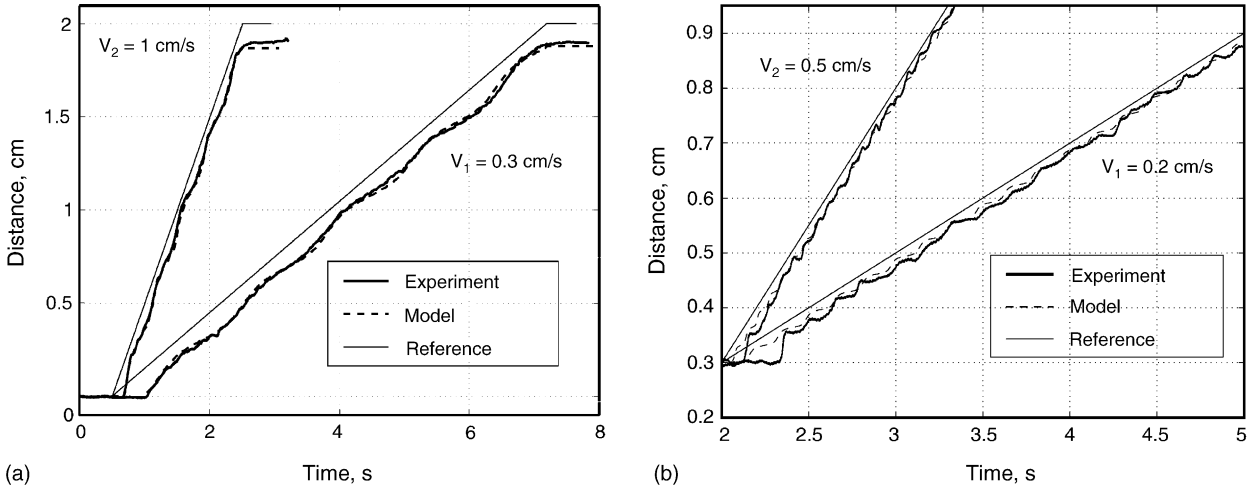

Fig. 11. Comparison of the model and experimental data on rotor translation in open-loop operation for two LSM designs. Driving current amplitude is $I_0 = 1.2$ A. Two different speeds are shown for each design. (a) LSM1, $V_1 = 0.3$ cm/s and $V_2 = 1$ cm/s; (b) LSM2, $V_1 = 0.2$ cm/s and $V_2 = 0.5$ cm/s.

frequency according to Eq. (1). Fig. 11(a) shows that for LSM1, the model data agrees well with experimental data. The straight reference line represents the position as given by the synchronous velocity. Key non-linear features of open-loop performance are: delayed translation at the beginning, undershoot in the steady-state position, and a wavy translational profile. The first two features are due to friction. The delay, a spatial lag, is analogous to angular lag between the rotor and the rotating stator field in rotary motors. The undershoot is due to the driving currents stopping when the reference reaches steady state. The wavy characteristic is due to the force ripples shown in Fig. 10(a), and occurs with a spatial periodicity equal to the width of one multiturn coil.

LSM2 exhibits the same three basic characteristics as LSM1. However, due to reduced pole pitch and reduced near-field effects in the stator field, the waves are reduced in amplitude. Though the model described in previous section does not account for interaction of permanent magnet and ferromagnetic core used in LSM2 design, experimental results agrees well with the model data. Six ripples per pole pitch shown in force distribution (Fig. 10(b)) are clearly seen in the translation plot.

5.2. Closed-loop control

To improve translation performance, both LSM designs were placed under closed-loop control. The immediate goals of closed-loop control are: (1) first, to minimize the error between the reference and rotor positions; (2) second, to minimize the over/undershoot due to friction; (3) to attenuate the wavy non-linearities due to fluctuations in the stator field; (4) and lastly, to compensate for any external disturbances and return the stage to its desired trajectory as quickly as possible.

Fig. 12 shows the block diagram of the LSM control system. The effective LSM input $u(t)$ (given as simply u in the diagram) defines the equilibrium position that the rotor follows. The current function $i_u(u(t))$ translates the equilibrium position demand into the appropriate three-phase current outputs that actuate the LSM. From input $u(t)$ to output $x_r(t)$, the effective LSM is a single-input–single-output (SISO) system controlled by C. For this, discussion feed forward gain is $K_{ff} = 2\pi/\tau$, and feedback gain is $K_{fb} = 1$. For open-loop operation, $C = 0$, and the LSM input $u(t) = K_{ff} r(t)$ is determined directly from the desired reference position $r(t)$. For closed-loop controlled operation of the LSM, the SISO controller, C, is a linear proportional integral derivative (PID) controller defined as:

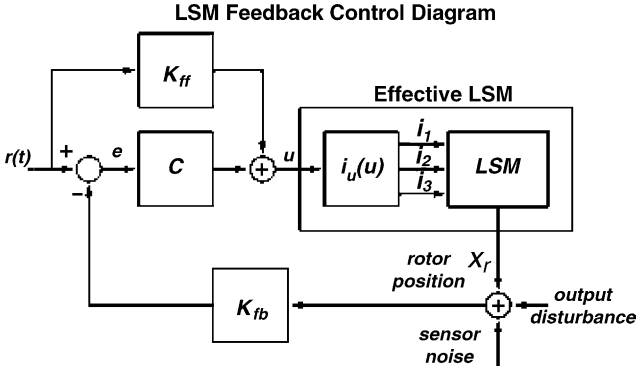

Fig. 12. Block diagram of LSM closed-loop control system.

$$C(t) = K_P e(t) + K_I \int_0^t e(t)\,dt + K_D \frac{de(t)}{dt}$$

where $e(t)$ is the error signal between the reference $r(t)$ and the output $x_r(t)$. The controller gains K_P, K_I, K_D were tuned heuristically online until desirable performance was achieved. The controller used is linear, and thus will not be able to completely remove the LSM non-linearities; however, it will be able to reduce their effect on the position trajectory of the LSM.

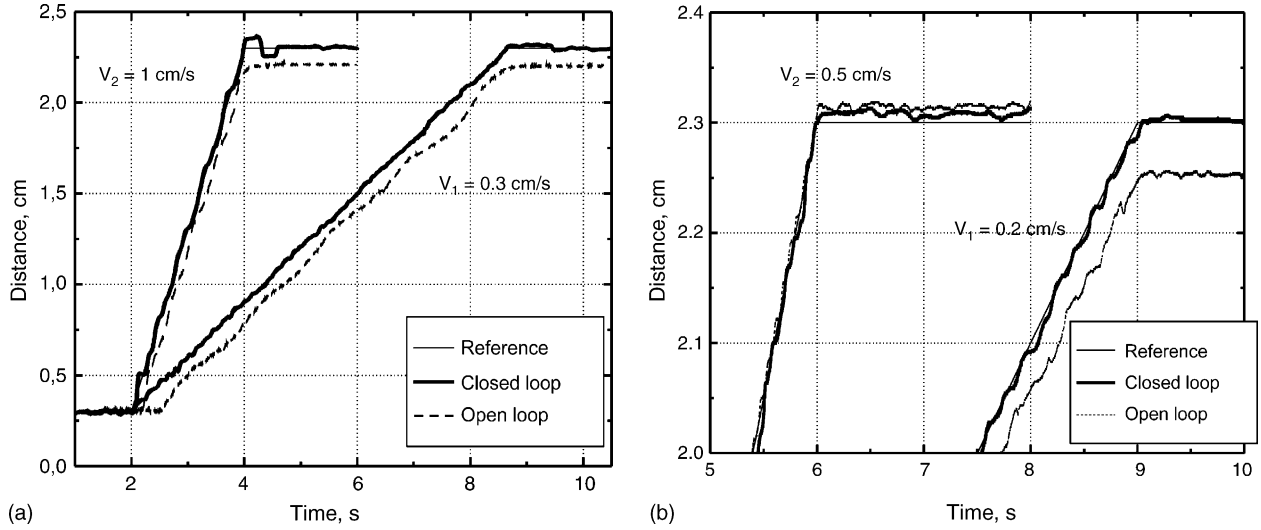

Fig. 13. Comparison of the open-loop and closed-loop performance for two LSM designs. Driving current amplitude is $I_0 = 1.2$ A. Two different speeds are shown for each design. (a) LSM1, $V_1 = 0.3$ cm/s and $V_2 = 1$ cm/s; (b) LSM2, $V_1 = 0.2$ cm/s and $V_2 = 0.5$ cm/s.

In Fig. 13, comparison of open- and closed-loop rotor translation at the conditions described in open-loop section is shown for both LSM designs. Examination of Fig. 13 shows that closed-loop control for both motors improved performance. Although attenuated, some wavy behavior persists as expected from the linear nature of the PID. Increasing the proportional gain of the controller can reduce deviations from the reference but at the cost of high-frequency oscillations and sensitivity to sensor noise. Increasing the integrator gain can make the system respond to overshoots of the stopped reference signal more quickly. However, the accumulation of constant error while the motor is in a stiction state causes the integrator to wind-up and overcorrect for the problem, leading to oscillations in the steady state; see Fig. 13(a). Controller inefficiency is more pronounced at high spead. Closed-loop data for LSM2 shows that with a better actuator design, there is less room for improvement with linear PID feedback control. Fig. 13(b) shows that the integral action of the PID controller is driving the steady-state error toward zero, while the open-loop position stays fixed. Also, the waves are attenuated and slightly more centered about the reference than in the open-loop case. An important issue is that it is impossible for the controller to remove the waves completely. As the controller has no a prior knowledge of the field fluctuations, they look like disturbances to which it must react. To fully remove the fluctuations, a more sophisticated position-dependent non-linear prefilter is required to minimize the stator field fluctuations.

6. Conclusions

This paper examined two design approaches to the miniature electromagnetic linear synchronous motors. The first approach, LSM1, utilized multiturn planar microcoils in conjunction with a 6-mm diameter commercial “button” magnet to produce a large actuation force. LSM1 represents the basic approach taken by previous reports on linear electromagnetic actuators. The second approach, LSM2, was based on screen-plated permanent magnets and a serpentine microcoil array, thus having the dual advantage of a fully microfabricated actuator and more precise and linear performance. An analytical dynamic model was developed and implemented to assess and compare the performance of the two design approaches. Comparison between simulation and experimental data of open-loop performance demonstrated the accuracy and value of the model. Through the model, it was found that fluctuating near-field effects of the translating stator field produced non-linear dynamic behavior. The model also showed that the near-field fluctuations were more significant in the multiturn coil design than the serpentine coil design, and the effect was larger force ripples and poorer position trajectory performance for LSM1. The smaller electromagnetic force of LSM2 due to weaker magnets and smaller force ripples due to smaller pole pitch and coil design were also shown by the model and corroborated by experimental data. A feedback control system using a heuristically tuned PID controller was employed to compensate for external disturbance forces such as friction, and to attenuate the effect of non-linear force ripples on positions trajectory performance of both LSM designs. The linear controller, while significantly improving the performance of both LSM designs over open-loop operation was unable to completely remove the effect of the non-linear force ripples. To enable micron scale precision positioning, these non-linearities must be dealt directly with a non-linear controller. An effective feedback linearization procedure has been developed for the LSM and tested in simulation. Present work involves implementing the non-linear controller and evaluating its performance on the experimental system. With such a controller, the performance goals of several miniature LSM applications can be realized.

References

[1] S.D. Collins, R.L. Smith, C. Gonzalez, K.P. Stewart, J.G. Hagopian, J.M. Sirota, Fourier-transform optical microsystems, Opt. Lett. 24 (12) (1999) 844–846.
[2] I. Hayashi, N. Iwatuki, Micro moving robotics, in: Proceedings of the 1998 International Symposium on Micromechatronics and Human Science, 1998, pp. 41–50.
[3] D.L. Polla, BioMEMS applications in medicine, in: Proceedings of the 2001 International Symposium on Micromechatronics and Human Science, 2001, pp. 13–15.
[4] Burleigh Industries, http://www.exfo.com/en/products/gf_Family104.asp.
[5] J.W. Judy, D.L. Polla, W.P. Robbins, A linear piezoelectric stepper motor with submicrometer step size and centimeter travel range, IEEE transactions on ultrasonics, ferroelectrics and frequency control, 37 (5) (1990) 428–437.
[6] R. Yeh, S. Hollar, K.S.J. Pister, Single mask, large force, and large displacement electrostatic linear inchworm motors, in: Proceedings of the 14th IEEE International Conference on Micro Electro Mechanical Systems, Technical Digest, MEMS 2001, 2001, pp. 260–264.
[7] B. Wagner, W. Benecke, Microfabricated actuator with moving permanent magnet, in: Proceedings of the 1991 IEEE MEMS Conference, Nara, Japan, 1991, pp. 27–32.
[8] B. Wagner, M. Kreutzer, W. Benecke, Permanent magnet micromotors on silicon substrates, J. MEMS 2 (1993) 23–29.
[9] H. Kube, V. Zoepping, R. Hermann, A. Hoffmann, E. Kallenbach, Electromagnetic miniactuators using thin magnetic layers, Smart Mater. Struct. 9 (2000) 336–341.
[10] C. Liu, Development of surface micromachined magnetic actuators using electroplated permalloy, Mechatronics 8 (1998) 613–633.
[11] Y. Shinozawa, T. Abe, T. Kondo, A proportional microvalve using a bi-stable magnetic actuator, in: Proceedings of the 1997 IEEE MEMS Conference, Nagoya, Japan, 1997, pp. 233–237.
[12] T.M. Liakopoulos, W. Zhang, C.H. Ahn, Micromachined thick permanent magnet arrays on silicon wafers, IEEE Trans. Magn. 32 (1996) 5154–5156.
[13] L.K. Lagorce, M.G. Allen, Magnetic and mechanical properties of micromachined strontium ferrite/polyimide composites, J. MEMS 6 (1997) 307–312.
[14] H. Nakazawa, Y. Watanabe, O. Morita, M. Edo, E. Yonezawa, The two-dimensional micro conveyer: principles and fabrication process of the actuator, in: Proceedings of International Solid State Sensors and Actuators Conference (Transducers ’97), 1997, pp. 33–36.

[15] T.-S. Chin, Permanent magnet films for applications in microelectromechanical systems, J. Mag. Mag. Mater. 209 (2000) 75–79.
[16] J.F. Gieras, Z.J. Piech, Linear Synchronous Motors: Transportation and Automation Systems, CRC Press, Boca Raton, 1999.
[17] C. Gonzalez, R.L. Smith, D.G. Howitt, S.D. Collins, MicroJoinery: concept, definition, and application to microsystem development, Sens. Actuators A A66 (1–3) (1998) 315–332.
[18] A.P. Wallace, D.W. Howard, J.S. Sirota, R.L. Smith, S.D. Collins, Long-range translation actuator, in: Proceedings of the SPIE Conference on Micro- and Nanotechnology for Biomedical and Environmental Applications, SPIE vol. 3912, 2000, pp. 158–165.
[19] I.W. Wolf, Electroplating of magnetic materials, J. Appl. Phys. 33 (3) (1962) 1152–1159.
[20] M.E. Henstock, E.S. Spencer-Timms, The composition of thin electrodeposited alloy films with special reference to nickel–iron, in: Proceedings of the 6th International Metal Finishing Conference, 1963, pp. 179–185.
[21] H.E. Knoepfel, Magnetic Fields, John Wiley & Sons Inc., New York, 2000.